Magnon-driven skyrmion dynamics in antiferromagnets: Effect of magnon polarization

Z. Jin,[1] C. Y. Meng,[1] T. T. Liu,[1] D. Y. Chen,[1] Z. Fan,[1] M. Zeng,[1] X. B. Lu,[1] X. S. Gao,[1] M. H. Qin,[1,*] and J.-M. Liu[1,2]

[1]*Guangdong Provincial Key Laboratory of Quantum Engineering and Quantum Materials and Institute for Advanced Materials, South China Academy of Advanced Optoelectronics, South China Normal University, Guangzhou 510006, China*

[2]*Laboratory of Solid State Microstructures, Nanjing University, Nanjing 210093, China*

(Received 1 March 2021; revised 1 August 2021; accepted 2 August 2021; published 13 August 2021)

Controllable magnetic skyrmion motion represents a highly relevant issue in preparing advanced skyrmion-based spintronic devices. Specifically, magnon-driven skyrmion motion can be easily accessible in both metallic and insulating magnets and thus is highly preferred over electric current control, further for the ultralow energy consumption. In this paper, we investigate extensively the dynamics of skyrmion motion driven by magnons in an antiferromagnet using the collective coordinate theory, focusing on the effect of magnon polarization. It is theoretically revealed that skyrmion Hall motion driven by circularly polarized magnons becomes inevitable generally, benefiting a comprehensive understanding of antiferromagnetic (AFM) skyrmion dynamics. More importantly, the elastic scattering theory and numerical results unveil the strong interdependence between linearly polarized magnons and skyrmion motion, suggesting the complicated dependence of skyrmion motion on the polarization nature of driving magnons. On the reversal, the scattering from the moving skyrmion may lead to decomposition of the linearly polarized magnon into two elliptically polarized magnon bands. Consequently, a net transverse force acting on the skyrmion is generated owing to the broken mirror symmetry, which in turn drives skyrmion Hall motion. Hall motion can be completely suppressed only in a specific condition where the mirror symmetry is preserved. This paper unveils nontrivial skyrmion-magnon scattering behavior in antiferromagnets, advancing AFM spintronics and benefiting high-performance devices.

DOI: 10.1103/PhysRevB.104.054419

I. INTRODUCTION

During the past decades, the dynamics of skyrmions [1] has attracted extensive attention for designing advanced skyrmion-based spintronic devices such as race-track memory and logic units [2,3]. Specifically, ferromagnetic skyrmions have been observed in a series of chiral magnets [4–8] and heavy metal/ferromagnetic films [9–12] with broken inversion symmetry. Subsequently, it has been demonstrated that skyrmion motion can be effectively driven by using various external stimuli including electric current [13,14], gradient magnetic field [15], oscillating and gradient electric field [16,17], and polarized magnons [18–26]. Among these stimuli, magnons as the quanta of spin waves, driving skyrmion motion without Joule heating due to the absence of charge physical transport, are particularly attractive for the advantage of low-energy consumption. In this case, polarized magnons are deflected by the fictitious magnetic field from skyrmions, which reversely drive skyrmion motion through the momenta exchange [18,27,28].

Alternatively, antiferromagnetic (AFM) skyrmions have been theoretically predicted [29,30] and experimentally observed in antiferromagnets with synthetic structures and three sublattices [31,32], which are of great interest in high-density and high-speed [33,34] spintronic devices. Specifically, an AFM skyrmion is comprised of two coupled spin structures with opposite topological numbers, resulting in strong anti-interference capability and ultrafast magnetic dynamics [35,36]. For example, it has been theoretically revealed that the speed of the AFM skyrmion is much larger than ferromagnetic skyrmions under the same electric current density [33]. Nevertheless, one may note that magnon driving rather than electric current control would be highly preferred, not only for energy saving, but also because magnon control works much better in insulating systems, considering that plenty of antiferromagnets are insulating. Therefore, an understanding of AFM skyrmion motion driven by polarized magnons becomes highly relevant.

Unlike the case in ferromagnets where magnons can only be right-circularly polarized, magnons in antiferromagnets can be both right- and left-circularly polarized, adding a polarization degree of freedom including all linear and elliptical polarizations [37,38]. Thus, magnon polarization could be used in modulating AFM skyrmion dynamics and even in encoding information in magnons. For instance, left- and right-handed magnons are deflected by AFM skyrmions toward opposite transverse directions due to their opposite effective charges, resulting in the magnon spin Hall effect. Consequently, circularly polarized magnons drive skyrmion Hall motion even in antiferromagnets. Furthermore, Hall motion highly depends on magnon polarization, which could be suppressed for linearly polarized magnons, attributing to the equal superposition of the left- and right-handed magnon bands, like current-driven AFM skyrmion motion [39].

*qinmh@scnu.edu.cn

These important works thus unveil interesting magnon-driven skyrmion dynamics, benefiting future spintronic and magnonic applications. However, the interplay between polarized magnons and AFM skyrmions could be more complex than supposed earlier [37]. Theoretically, linearly polarized magnons could be decomposed into magnon bands with elliptical polarizations, which breaks the mirror symmetry of scattered spin-wave channels and generates a net transverse force on the topological spin texture. In this case, different spin dynamics such as skyrmion Hall motion could be also induced by linearly polarized magnons. As a matter of fact, a strong dependence of AFM domain wall motion on the polarization of the injected magnons has been revealed [40–42]. In the presence of the Dzyaloshinskii-Moriya interaction (DMI), magnons with out-of-plane linear polarization drive the wall forward, while in-plane linearly polarized magnons propagate through the wall almost freely [40]. To some extent, strong interdependence between linearly polarized magnons and AFM skyrmion motion is expected, considering the relevance between these noncollinear magnetic textures. Thus, the effect of magnon polarization on AFM skyrmion dynamics deserves to be further clarified, considering its importance in AFM spintronics and magnonics.

In this paper, we investigate AFM skyrmion dynamics driven by injected magnons using theoretical analysis and Landau-Lifshitz-Gilbert (LLG) simulations, focusing on the effect of magnon polarization. The skyrmion motion equation driven by circularly polarized magnons is derived based on the collective coordinate theory, clarifying the physics underlying the numerical simulations. In addition, strong interdependence between linearly polarized magnons and skyrmion longitudinal motion is theoretically and numerically revealed, allowing a comprehensive understanding of the driving mechanism. More importantly, we numerically demonstrate that linearly polarized magnons are generally decomposed into two elliptically polarized magnon bands with opposite handedness. As a result, a net transverse force is induced owing to the broken mirror symmetry, which in turn drives skyrmion Hall motion.

II. MODEL AND METHODS

Like the earlier work [43], we study a two-dimensional AFM model in the xy plane with two magnetic sublattices that have magnetic moments $\mathbf{m}_1$ and $\mathbf{m}_2$, respectively, satisfying condition $|\mathbf{m}_1| = |\mathbf{m}_2| = S$, with spin length S. The normalized staggered Néel vector $\mathbf{n}$ is defined as $\mathbf{n} = (\mathbf{m}_1 - \mathbf{m}_2)/2S$ [44] to describe the Lagrangian. Considering the exchange energy, the anisotropy energy, and the interfacial DMI, one has the Lagrangian density L [45]:

$$L = \frac{\rho_0^2}{2A_0}\dot{\mathbf{n}}^2 - u_0, \tag{1}$$

with the thermodynamic free energy:

$$u_0 = \frac{A^*(\nabla \mathbf{n})^2}{2} - \frac{K n_z^2}{2} + \frac{D[n_z \nabla \cdot \mathbf{n} - (\mathbf{n} \cdot \nabla) n_z]}{2}, \tag{2}$$

where A_0 and A^* are the homogeneous and effective exchange constants, respectively, K is the easy z-axis anisotropy constant, D is the DMI constant, and $\rho_0 = \hbar S/a$ is the density of the staggered spin angular momentum per unit cell [46], with the lattice constant a and reduced Planck's constant $\hbar$.

To describe the magnons, it is convenient to use a global frame defined by three mutually orthogonal unit vectors $(\mathbf{e}_1, \mathbf{e}_2, \mathbf{e}_3)$ with $\mathbf{e}_3 = \mathbf{n}_0/|\mathbf{n}_0| = \mathbf{e}_1 \times \mathbf{e}_2$ where $\mathbf{n}_0$ is the equilibrium configuration. A weakly excited state can be parametrized as $\mathbf{n} = \mathbf{n_0} + \delta_x \mathbf{e}_1 + \delta_y \mathbf{e}_2$, where δ_x and δ_y describe the amplitude components of the magnon. Then one obtains the two monochromatic solutions with the complex fields $\psi^* = \delta_x \pm i\delta_y$ for right/left circularly polarized magnon modes, which corresponds to the anticlockwise/clockwise precession of $\mathbf{n}$ [47]. Moreover, the complex field can also be rewritten in the form of plane wave $\psi = \exp[i(\boldsymbol{k} \cdot \boldsymbol{r} - \omega t)]$, where $\boldsymbol{k}$ is the wave vector, $\boldsymbol{r}$ is the position vector with length r and polar angle ϑ, and ω and t are frequency and time, respectively.

Subsequently, the skyrmion dynamics driven by polarized magnons is analytically calculated using the collective coordinate and elastic scattering theories. Moreover, the position and velocity of the skyrmion are also estimated using LLG simulations of the discrete spin model to check the validity of the theoretical analysis. LLG simulation details are presented in Appendix A.

III. RESULTS AND DISCUSSION

A. Hall motion of skyrmions driven by circularly polarized magnons

In this part, a scheme of collective coordinates for magnons and skyrmions in a Lagrangian frame is used to formulate the skyrmion dynamics driven by circularly polarized magnons. Following the earlier work [25], we transform the z axis to the equilibrium configuration $\mathbf{n}_0$ using the rotation matrix $\mathbf{T}$ satisfying $\mathbf{n}_0 = \mathbf{T}\mathbf{n}_0'$, with $\mathbf{n}_0' = \mathbf{e}_z$, where $\mathbf{e}_z$ is the unit vector along the z axis [48–50], to conveniently derive the emergent electromagnetic field.

The Lagrangian density L can be divided into three parts: L_0 from the equilibrium texture, $L_{\rm sw}$ from the disturbance part, and $L_{\rm int}$ from the skyrmion-magnon interactions (the detailed derivation is presented in Appendix B):

$$\begin{aligned} L_0 &= \frac{(\rho_0 \partial_t \mathbf{n}_0)^2}{2A_0} - u_0, \\ L_{\rm sw} &= \frac{\rho_0^2 (\partial_t \psi^* \partial_t \psi)}{2A_0} - \frac{A^* (\partial_i \psi^* \partial_i \psi)}{2} + \frac{K(\psi^* \psi)}{2}, \\ L_{\rm int} &= -\frac{i\rho_0^2 (\psi^* \partial_t \psi - \psi \partial_t \psi^*) a_t^0}{2A_0} - \mathbf{j} \cdot \boldsymbol{a}_{\rm total} + \psi^* \psi u_0 \\ &\quad - \frac{\psi^* \psi (\rho_0 \partial_t \mathbf{n}_0)^2}{2A_0}, \end{aligned} \tag{3}$$

where $i = 1$, 2, and 3 denote the spatial derivatives with respect to the x, y, and z axes, respectively. Here, $a_t^0 = -\cos\theta \cdot \partial_t \varphi$ [25,49,51,52] coincides with the geometrical scalar potential due to the basis variation, θ and φ are the polarization angle and azimuth angle of $\mathbf{n}$, respectively, $\boldsymbol{a}_{\rm total} = \boldsymbol{a}^0 + \boldsymbol{a}_{\rm D}$ [49] is the total vector potential including the contributions from the inhomogeneous magnetization

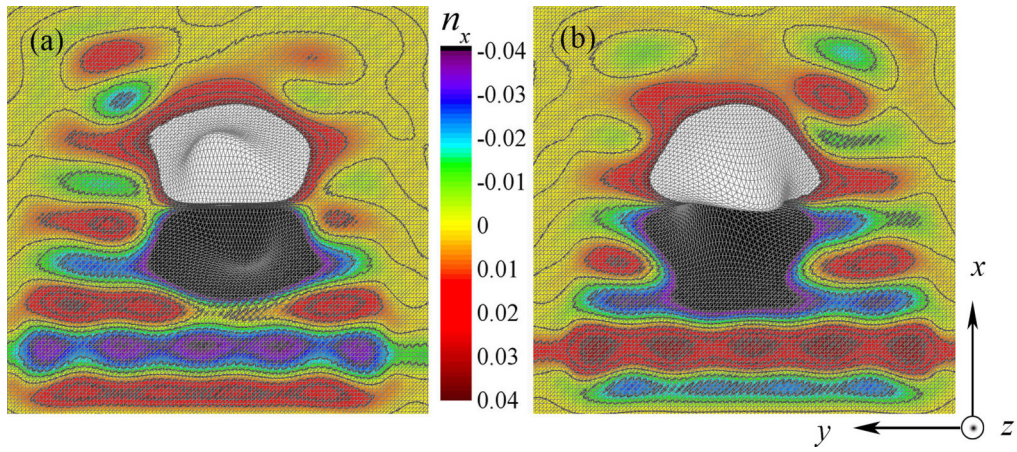

FIG. 1. The spatial map of n_x for the (a) left-circularly and (b) right-circularly polarized magnons injected from the bottom of the frame and scattered by the AFM skyrmion (the black and white part).

$\boldsymbol{a}^0 = -\cos\theta \cdot \nabla\varphi$ and from the DMI $\boldsymbol{a}_{\rm D} = -(D/2A^*)\mathbf{n}_0$, and $\mathbf{j} = -iA^*(\psi^*\nabla\psi - \psi\nabla\psi^*)/2$ is the spin wave flux.

For a stable skyrmion whose position is characterized by $\mathbf{X} = \{X_i\}$, Thiele theory is used to describe its dynamics. Moreover, one may use a set of collective coordinates $\mathbf{x} = \{x_u\}$ to characterize the position of a spin-wave packet [25] and to estimate the magnon group velocity $\partial\omega/\partial\boldsymbol{k}$. Then the full Lagrangian L_z can be rewritten in terms of $\{X_i\}$ and $\{x_u\}$:

$$L_z = M^{ij}\dot{X}_i^2 - \frac{2\omega A_i^0 \dot{X}_i}{A_0} - U_0 + \rho\left[\frac{(\rho_0\omega)^2}{A_0} - A^*\boldsymbol{k}^2\right] - 2\rho A^*\boldsymbol{a}_{\rm total}\cdot\boldsymbol{k}, \tag{4}$$

where the Einstein summation rules over the repeated indices, $M^{ij} = (1-2\rho)\rho_0^2\int dV(\partial_i\mathbf{n}_0\cdot\partial_j\mathbf{n}_0)/2A_0$ is the dissipative tensor describing the effective mass [53] due to the exchange interaction between neighboring spins, $\dot{X}$ represents the derivative with respect to time, $U_0 = \int dV(1-\psi\psi^*)u_0$ is the total texture energy, $A_i^0 = \rho_0^2\int dV\psi\psi^* a_i^0/2$, and $\rho = \int dV\psi\psi^*/2$ is the total spin wave intensity.

Similarly, the Rayleigh function is rewritten as

$$R = \frac{\alpha}{2}\left[\frac{2A_0}{\rho_0^2}M^{ij}\dot{X}_i\dot{X}_j + \left(\frac{\omega^2}{2A^*}\right)\psi^*\psi\dot{x}_u^2\right]. \tag{5}$$

After applying the Euler-Lagrange rule, we obtain two coupled equations to describe the dynamics of skyrmions and magnons:

$$2M^{ij}\ddot{X}_j + \partial_i U_0 + 2\omega\left(\frac{\partial A_j^0}{\partial X_i} - \frac{\partial A_i^0}{\partial X_j}\right)\frac{\dot{X}_j}{A_0} + \frac{2\alpha A_0 M^{ij}\dot{X}_j}{\rho_0^2} = -2\rho\omega\rho_0^2\left(\frac{\partial a_v}{\partial X_i} - \frac{\partial a_i}{\partial x_v}\right)\frac{\dot{x}_v}{A_0}, \tag{6a}$$

$$\frac{2\rho_0^4\omega^2}{A_0^2A^*}\ddot{x}_u - 2\partial_u u_0 + 2\frac{\rho_0^2\omega}{A_0}\left(\frac{\partial a_v^0}{\partial x_u} - \frac{\partial a_u^0}{\partial x_v}\right)\dot{x}_v + \frac{\alpha\omega^2}{A^*}\dot{x}_u = 2\omega\left(\frac{\partial a_u}{\partial X_j} - \frac{\partial a_j}{\partial x_u}\right)\frac{\dot{X}_j}{A_0}. \tag{6b}$$

To some extent, magnon scattering is equivalent to the classical motion of a massive particle subjecting to dissipation-induced friction and effective magnetic field from the skyrmion. Particularly, the third term in the left side of Eq. (6b) is associated with the effective Lorentz force acting on the spin-wave packet, which induces transverse motion of the packet. Moreover, the effective field is reversed when the sign of ω is changed, resulting in the topological spin Hall effect, as demonstrated in Fig. 1, where the LLG simulated spatial map of n_x is presented. It is clearly shown that the left-circularly polarized magnons with $\omega > 0$ are deflected to the left side [Fig. 1(a)] by the skyrmion, while the right-handed magnons with $\omega < 0$ are deflected to the right side [Fig. 1(b)].

For an injected magnon current, Eq. (6a) is updated to

$$2M^{ij}\ddot{\mathbf{X}} + \partial_i U_0 + \frac{\dot{\mathbf{X}}\times 2\omega\rho(4\pi Q\cdot\mathbf{e}_z)}{A_0} + \frac{2\alpha A_0 M^{ij}\dot{\mathbf{X}}}{\rho_0^2} = -\frac{2\rho\omega\rho_0^2\dot{\mathbf{x}}\times(4\pi Q\cdot\mathbf{e}_z)}{A_0}, \tag{7}$$

where $\ddot{\mathbf{X}}$ is the second-order derivative with respect to time, and $Q = \int dV(\nabla\times\boldsymbol{a}^0)_z/4\pi$ is the staggered topological charge. It is noted that the right term is the driving force acting on the skyrmion from the injected magnons, which can be divided into the longitudinal (x direction) and transverse

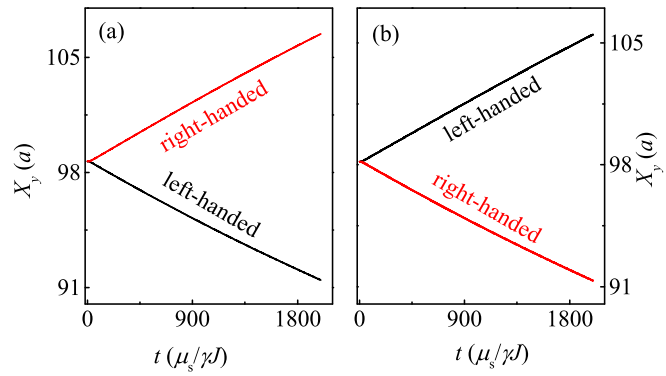

FIG. 2. The temporal evolution of the position X_y of (a) skyrmion and (b) antiskyrmion for the left- and right-handed polarized magnons.

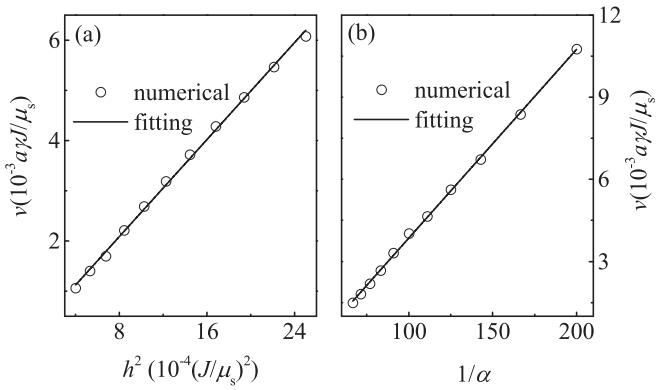

FIG. 3. The simulated (empty circles) and fitted (solid line) skyrmion speeds v as functions of (a) h^2 for $\alpha = 0.01$ with fitted slope 2.4×10^{-4}, and (b) $1/\alpha$ for $h = 0.04\,J/\mu_s$ with fitted slope 0.69×10^{-4}.

(y direction) parts. Thus, both the transverse driving force and the Magnus force (the third term in the left side) are reversed for opposite ω [39,54] or opposite Q due to the topological spin Hall effect, resulting in skyrmion Hall motion whose direction is determined by the magnon handedness and skyrmion charge.

To some extent, magnon-skyrmion scattering could be related to an analog of electrons passing through the magnetic field. Specifically, the handedness of the magnon corresponds to the sign of effective charge, while the topological charge of the skyrmion determines the direction of the fictitious magnetic field. The dependences of skyrmion Hall motion on ω and Q are verified by the LLG simulations. Figure 2(a) shows the temporal evolution of the transverse position of the skyrmion, demonstrating that opposite transverse motions are driven by the left- and right-handed magnons, respectively. Furthermore, for an antiskyrmion with an opposite Q stabilized by anisotropic DMI [55,56], the magnons drive transverse motion opposite to that of the skyrmion, corresponding to isotropic DMI, as shown in Fig. 2(b).

Considering stable motion with negligible deformation of the skyrmion and neglecting $\partial_i U_0$, the solution of Eq. (7) gives the skyrmion velocity:

$$\mathbf{v} = \frac{\rho_0^2 \rho \mathbf{F}_m}{A_0 \alpha M^{ij}}, \tag{8}$$

where ρ is square related to magnetic field h used to generate magnons [57], and $\mathbf{F}_m = 4\pi\omega\rho_0^2\dot{\mathbf{x}}\times(Q\cdot\mathbf{e}_z) + 4\pi\omega\mathbf{v}\times(Q\cdot\mathbf{e}_z)$ is the driving force. Thus, linear dependences of the skyrmion speed v on h^2 and $1/\alpha$ are expected for a weak field.

To check the validity of the theory, the dependences of v on various parameters are numerically simulated and analytically fitted. Figure 3(a) gives the simulated v for various h^2, clearly demonstrating a linear relation. It is noted that the driving force on the skyrmion is linearly correlated with h^2, resulting in the linear dependence of v on h^2. On the other hand, skyrmion mobility is reduced by an enhanced damping term, resulting in the decrease of v with the increasing α, as shown in Fig. 3(b), which clearly demonstrates the linear relation between v and $1/\alpha$. Moreover, the speed of an AFM skyrmion is expected to be larger than a ferromagnetic skyrmion because the magnons in antiferromagnets operate in the terahertz regime, which is orders of magnitude higher than in typical ferromagnets. Taking $a = 1$ nm, $J = 6.59\times10^{-12}$ J/m, and $\mu_s \approx 1.7\,\mu_B$ as an example, the velocity is estimated to be ~ 370 m/s for $\alpha = 0.001$ under $h = 0.04\,J/\mu_s$.

B. Longitudinal velocity of skyrmions driven by linearly polarized magnons

In this section, we analytically investigate the skyrmion longitudinal velocity v_x driven by linearly polarized magnons. Here, the remaining massive fluctuation modes are represented by the dimensionless staggered field δ. The Néel vector is expressed as

$$\begin{aligned} n_x &= \left(2\sin^2\frac{\theta}{2}\cos^2\varphi - 1\right)\delta_x + 2\sin^2\frac{\theta}{2}\cos\varphi\sin\varphi\delta_y \\ &\quad + \sin\theta\cos\varphi\delta_z, \\ n_y &= 2\sin^2\frac{\theta}{2}\cos\varphi\sin\varphi\delta_x + \left(2\sin^2\frac{\theta}{2}\sin^2\varphi - 1\right)\delta_y \\ &\quad + \sin\theta\sin\varphi\delta_z, \\ n_z &= \sin\theta\cos\varphi\delta_x + \sin\theta\sin\varphi\delta_y + \cos\theta\delta_z, \end{aligned} \tag{9}$$

with $\delta_z = (1-\delta_x^2-\delta_y^2)^{1/2}$.

First, we study skyrmion motion driven by x- and y-linearly polarized magnons. Considering an elastic scattering process, substituting Eq. (9) into Eq. (1) and conserving the second order in the fluctuation field, one obtains the Hamiltonian densities for the x- and y-linear polarizations L_x and L_y:

$$\begin{aligned} L_x &= \frac{\delta_x H_x \delta_x}{2} + \frac{\rho_0^2\dot{\delta}_x^2}{2A_0}, \\ L_y &= \frac{\delta_y H_y \delta_y}{2} + \frac{\rho_0^2\dot{\delta}_y^2}{2A_0}, \end{aligned} \tag{10}$$

with the Hamiltonians H_x and H_y, respectively:

$$\begin{aligned} H_x &= -A^*\left[-\sin^2\varphi(\partial_r\theta)^2 + \frac{2\cos\theta(\cos\theta-1)+\sin^2\theta\sin^2\varphi}{r^2}\right] + A^*\nabla^2 - D\left[-\sin^2\varphi\partial_r\theta + \frac{\sin\theta(1-\cos\theta-\cos\theta\cos^2\varphi)}{r}\right] \\ &\quad + K(\sin^2\theta\cos^2\varphi - \cos^2\theta), \\ H_y &= -A^*\left[-\cos^2\varphi(\partial_r\theta)^2 + \frac{2\cos\theta(\cos\theta-1)+\sin^2\theta\cos^2\varphi}{r^2}\right] + A^*\nabla^2 - D\left[-\cos^2\varphi\partial_r\theta + \frac{\sin\theta(1-\cos\theta-\cos\theta\sin^2\varphi)}{r}\right] \\ &\quad + K(\sin^2\theta\sin^2\varphi - \cos^2\theta). \end{aligned} \tag{11}$$

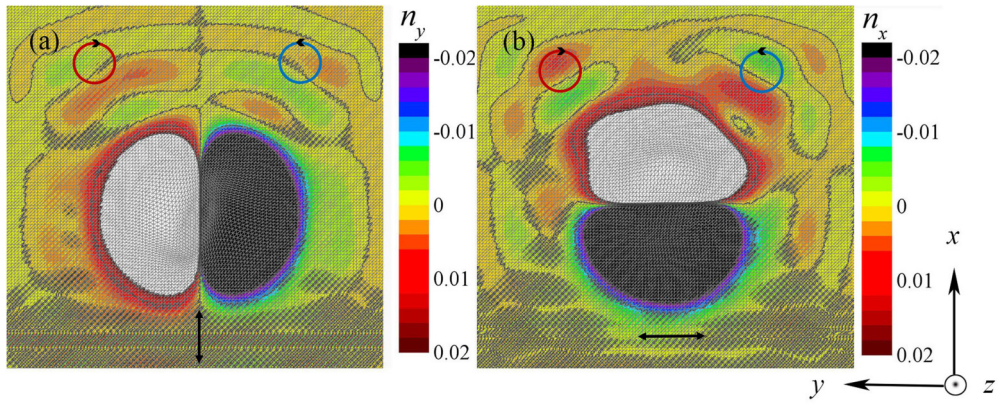

FIG. 4. Spatial map of (a) n_y for the x-linearly and (b) n_x for the y-linearly polarized magnons scattered by the skyrmion. The bidirectional arrows and circles depict the injected linearly and scattered circularly polarized spin waves, respectively.

Applying the Euler-Lagrangian equation, we obtain the dynamic equations for the x- and y-linearly polarized magnons, respectively:

$$\frac{\rho_0^2\ddot{\delta}_x}{A_0} = H_x\delta_x, \quad \frac{\rho_0^2\ddot{\delta}_y}{A_0} = H_y\delta_y. \tag{12}$$

Considering the excited spin wave with a fixed frequency, solving the dynamic equation becomes computing the eigenproblem of $-H_{xy}\delta_{xy} = \rho_0^2\omega^2\delta_{xy}/A_0$. Here, the scattering potential is calculated to be $H_{sx,sy} = -H_0 - H_{x,y}$, where $H_0 = -A^*\nabla^2 + K$ is the ground-state Hamiltonian. Thus, the difference between H_{sx} and H_{sy} could lead to different magnon scattering behaviors and skyrmion longitudinal velocities.

It is worth noting that the elastic scattering process with an unchanged magnon polarization is considered in the derivation of the Lagrangian density, which is inconsistent with the fact that the linearly polarized magnon is generally decomposed into circularly or elliptically polarized magnon bands by the skyrmion. However, the analytical argument on the skyrmion longitudinal velocity also works in such an inelastic scattering process, qualitatively at least. For example, different scattered magnon amplitudes for the x- and y-linear polarizations are observed in the LLG simulations, as shown in Fig. 4 where the spatial evolution of the **n** components are plotted. It is clearly shown that the linearly polarized magnons are decomposed into the left- and right-handed magnon bands, while the scattered magnon amplitude for the y-linear polarization [Fig. 4(b)] is obviously larger than that for the x-linear polarization [Fig. 4(a)].

Consequently, v_x is also dependent on the linear polarization direction of the injected magnons because the driving force is related to the scattered magnon amplitude. In Fig. 5(a), the simulated X_x (solid lines with the Néel skyrmion helicity $\eta = 0$, and ϕ is the angle between the polarization direction and the x axis) driven by the x- and y-linearly polarized magnons are presented, demonstrating that v_x for the y-linear polarization with $\phi = \pi/2$ is much larger than the x-linear polarization with $\phi = \pi$, which is consistent with the magnon scattering behaviors.

Generally, the skyrmion scattering potential H_s depending on ϕ reads

$$\begin{aligned} H_s = A^*&\left[-\sin^2(\vartheta+\phi+\eta)(\partial_r\theta)^2 + \frac{2\cos\theta(\cos\theta-1)+\sin^2\theta\sin^2(\vartheta+\phi+\eta)}{r^2}\right] \\ &+ D\left(-\sin^2(\vartheta+\phi+\eta)\partial_r\theta + \frac{\sin\theta\{1-\cos\theta-\cos\theta[1-\sin^2(\vartheta+\phi+\eta)]\}}{r}\right) \\ &- K\{\sin^2\theta[1-\sin^2(\vartheta+\phi+\eta)] - \cos^2\theta + 1\}. \end{aligned} \tag{13}$$

Thus, equal $\eta + \phi$ will result in the same v_x, which has been confirmed in the LLG simulated X_x of the Bloch skyrmion with $\eta = \pi/2$, as shown in Fig. 5(a) (dashed lines). It is clearly shown that v_x of the Bloch skyrmion driven by the x-/y-linearly polarized magnons is the same as that of the Néel skyrmion driven by y-/x-linearly polarized magnons, confirming the above theoretical argument.

As a matter of fact, v_x depending on ϕ could be reasonably assumed to be $v_x = C_1\sin^2(\vartheta+\eta+\phi) + C_2$, with the parameters C_1 and C_2 independent of ϕ, noting that the momentum transfer between skyrmions and magnons is mainly determined by the scattering potential. The LLG simulated v_x for various ϕ are summarized in Fig. 5(b), which can be well fitted by this equation ($C_1 = 5.6\times10^{-4}$ and $C_2 = 6.7\times10^{-4}$), further confirming the validity of the elastic theory in studying skyrmion longitudinal velocity driven by linearly polarized magnons.

C. Transverse velocity of skyrmions driven by linearly polarized magnons

Different from the earlier viewpoint, skyrmion Hall motion driven by linearly polarized magnons is generally observed,

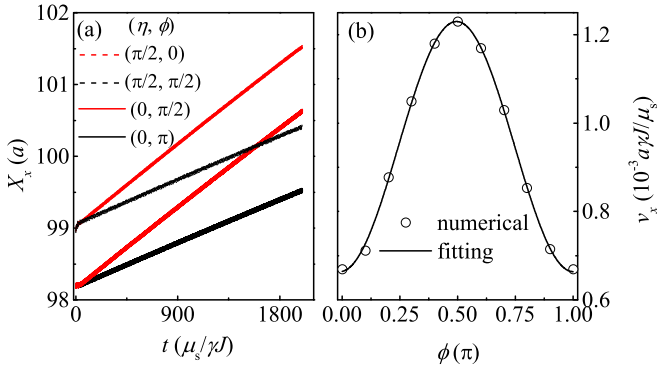

FIG. 5. (a) The position X_x of the Néel skyrmion with $\eta = 0$ (solid lines) and Bloch skyrmion with $\eta = \pi/2$ (dashed lines) as functions of time driven by the x ($\phi = 0$ or π) and y ($\phi = \pi/2$) linearly polarized magnons. (b) The simulated (empty circles) and analytically fitted (solid line) v_x as functions of ϕ.

as shown in Fig. 6(a), which gives the LLG simulated evolutions of X_y for $\phi = 0.8\pi$ and 0.9π. It is demonstrated that transverse motion is rather considerable and dependent on the polarization direction. In Fig. 6(b), the simulated transverse velocity v_y as a function of ϕ is presented, exhibiting a sinusoidal dependence of v_y on 2ϕ. This behavior is contrary to the earlier conclusion that the AFM skyrmion has no transverse motion when the injected magnons are linearly polarized.

To understand this unexpected phenomenon, we trace the local magnetization precession trajectories at different positions and give the results in Fig. 7. Unlike the earlier assumption that linearly polarized magnons are generally decomposed into circularly polarized magnon bands, the simulations clearly demonstrate that the injected magnons are decomposed into two elliptically polarized magnon bands with opposite handedness, as shown in Figs. 7(a) and 7(b), where we present the local magnetization precession trajectories for $\phi = 0.8\pi$.

In this case, the left-/right-handed magnons scattered by the skyrmion can be described by $\psi_{r/l} = A_1\cos(\boldsymbol{k}\cdot\boldsymbol{x} - \omega t \mp \varphi_0)\mathbf{n}'_x + A_2\cos(\boldsymbol{k}\cdot\boldsymbol{x} - \omega t)\mathbf{n}'_y$, with the ϕ-dependent amplitudes A_1 and A_2, and the phase φ_0, as demonstrated in Figs. 7(c) and 7(d), where we give the local

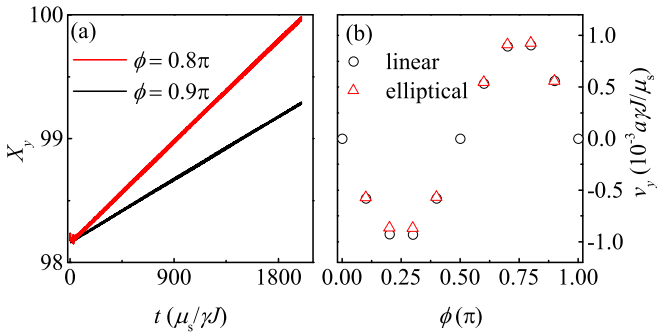

FIG. 6. (a) The evolutions of X_y for $\phi = 0.8\pi$ and 0.9π, and (b) the simulated v_y as functions of ϕ driven by the linearly polarized magnons (black empty circles) and by isolated elliptically polarized magnons (red empty triangles).

magnetization precession trajectories for $\phi = 0.9\pi$. Thus, the decomposed magnon bands break the mirror symmetry of scattered spin-wave channels and in turn generate a net transverse force acting on the skyrmion, resulting in skyrmion transverse velocity. As a matter of fact, the transverse velocity driven by two isolated magnon currents with left- and right-hand elliptical polarizations is also simulated, and the results are also given in Fig. 6(b). The good consistency between the simulated v_y for the linear polarization and elliptical polarizations strongly supports the revealed skyrmion-magnon scattering picture.

Particularly, for y- and x-linearly polarized magnons, the decomposed spin waves are parameterized by $\psi_{r/l} = A\cos(\boldsymbol{k}\cdot\boldsymbol{x} - \omega t \mp \pi/2)\mathbf{n}'_x + A\cos(\boldsymbol{k}\cdot\boldsymbol{x} - \omega t)\mathbf{n}'_y$ and $\psi_{r/l} = A\cos(\boldsymbol{k}\cdot\boldsymbol{x} - \omega t)\mathbf{n}'_x + A\cos(\boldsymbol{k}\cdot\boldsymbol{x} - \omega t \mp \pi/2)\mathbf{n}'_y$, respectively, which are exactly the circularly polarized magnons. In each case, the mirror symmetry of scattered spin-wave channels is preserved, and the transverse forces from the left- and right-handed magnon bands are perfectly canceled out, resulting in the suppression of skyrmion Hall motion [37].

To some extent, the phenomenon of injected magnons scattered by magnetic textures such as domain walls and skyrmions are like optical waves interacting with a retarder or wave plate, as has been revealed in an earlier report [41]. In this case, the decomposition of linearly polarized magnons depends on the magnon polarization and the helicity of the skyrmion. Specifically, the decomposition into circularly polarized magnons occurs for the angle between the polarization and helicity $(\phi - \eta) = 0$ or $\pi/2$, while the injected magnons are decomposed into elliptically polarized magnon bands for other $(\phi - \eta)$, as revealed in our numerical simulations.

Indeed, the skyrmion Hall effect may prohibit precise control of skyrmion motion, which goes against future applications. Interestingly, electric current drives AFM skyrmion motion straight along the current direction without path deviation, making AFM skyrmions attractive to device design. However, electric current control is deficient for energy loss

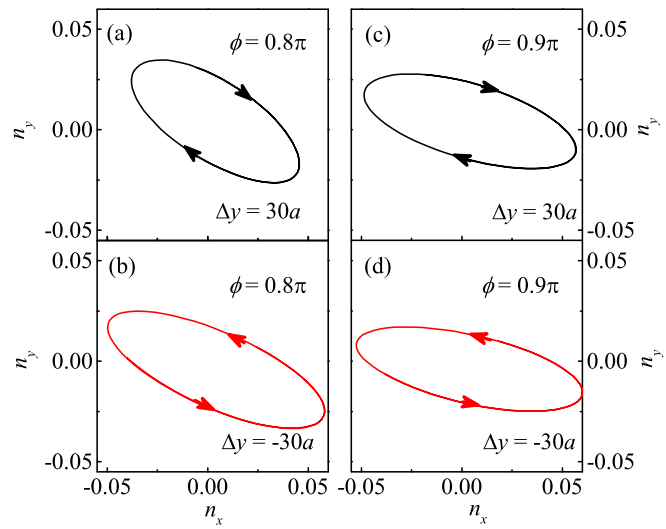

FIG. 7. The local magnetization-precession trajectory at different positions for (a) and (b) $\phi = 0.8\pi$ and (c) and (d) $\phi = 0.9\pi$.

and only works in metallic antiferromagnets, and thus, other energy-saving controls such as using polarized magnons are highly preferred. Importantly, the current simulations suggest that linear polarization of injected magnons should be delicately tuned to completely diminish skyrmion Hall effects. Thus, this paper further clarifies the complex interplay between skyrmions and polarized magnons in antiferromagnets, which is very meaningful for spintronic and magnonic applications.

IV. CONCLUSIONS

In conclusion, we have studied skyrmion dynamics driven by polarized magnons in antiferromagnets using analytical methods and numerical simulations. Skyrmion Hall motion driven by circularly polarized magnons is explained based on the collective coordinate theory. In addition, skyrmion longitudinal velocity strongly depending on the linear polarization of the injected magnons is revealed analytically and numerically. More importantly, we demonstrate that linearly polarized magnons are generally decomposed into elliptical magnon bands, which drives skyrmion Hall motion owing to the broken mirror symmetry. Thus, this paper unveils skyrmion-magnon scattering mechanisms in antiferromagnets, benefiting future spintronic applications.

ACKNOWLEDGMENTS

We sincerely appreciate insightful discussions with Huaiyang Yuan, Jin Lan, Zhengren Yan, and Weihao Li. This paper is supported by the Natural Science Foundation of China (Grants No. 51971096 and No. 51721001), the Natural Science Foundation of Guangdong Province (Grant No. 2019A1515011028), the Science and Technology Planning Project of Guangzhou in China (Grant No. 201904010019), and Special Funds for the Cultivation of Guangdong College Students Scientific and Technological Innovation (Grant No. pdjh2020a0148).

APPENDIX A: NUMERICAL SIMULATIONS OF THE ATOMISTIC SPIN MODEL

To check the validity of the theory, we also perform numerical simulations of the discrete model. Here, the two-dimensional Hamiltonian of the atomistic spin model is given by

$$H = J\sum_{\langle i,j\rangle}\mathbf{S}_i\cdot\mathbf{S}_j - D_0\sum_i(\mathbf{S}_i\cdot\mathbf{S}_{i+x}\times\mathbf{e}_y - \mathbf{S}_i\cdot\mathbf{S}_{i+y}\times\mathbf{e}_x) - K_0\left(S_i^z\right)^2, \tag{A1}$$

where the first term is the exchange interaction with $J = 1$ between the nearest neighbor spins, the second term is the DMI with $D_0 = 0.11J$ and the unit vector $\mathbf{e}_{x/y}$ along the x/y axis, and the last term is the anisotropy energy with $K_0 = 0.02J$. Experimentally, take the lattice constant $a = 1$ nm and $J = 6.59\times10^{-12}$ J/m as an example. The values of DMI and anisotropy constant are 7.25×10^{-4} J/m^2 and 1.32×10^{5} J/m^3, respectively, which are comparable with those in $KMnF_3$ [33]. The dynamics of the AFM skyrmion is investigated by solving the LLG equation:

$$\frac{\partial\mathbf{S}_i}{\partial t} = -\gamma\mathbf{S}_i\times\mathbf{H}_i + \alpha\mathbf{S}_i\times\frac{\partial\mathbf{S}_i}{\partial t}, \tag{A2}$$

where $\mathbf{H}_i = -\mu_s^{-1}\partial H/\partial\mathbf{S}_i$ is the effective field, and $\alpha = 0.01$ is the damping constant. We use the fourth-order Runge-Kutta method to solve the LLG equation on a 200×200 square lattice.

The magnons are excited by applying the AC magnetic field locally in the region of $60 \leqslant x < 64$ and $0 < y \leqslant 200$. Specifically, we generate right-/left-handed magnons by applying AC magnetic field $\boldsymbol{h}_R/\boldsymbol{h}_L = h[\cos(\omega_0 t)\mathbf{e}_x \pm \sin(\omega_0 t)\mathbf{e}_y]$ with the frequency ω_0. Similarly, the y- and x-linearly polarized magnons are generated by applying $\boldsymbol{h}_x = h\cos(\omega_0 t)\mathbf{e}_y$ and $\boldsymbol{h}_y = h\sin(\omega_0 t)\mathbf{e}_x$, respectively. The absorbing boundary conditions are used to eliminate the reflection of the magnons at the boundary. The position of the skyrmion $\mathbf{X}$ is estimated by [20]

$$X_i = \frac{\int[i\mathbf{n}\cdot(\partial_x\mathbf{n}\times\partial_y\mathbf{n})]dxdy}{\int[\mathbf{n}\cdot(\partial_x\mathbf{n}\times\partial_y\mathbf{n})]dxdy}, \quad i = x, y. \tag{A3}$$

Then the velocity is numerically calculated by $\mathbf{v} = d\mathbf{X}/dt$.

APPENDIX B: THE DERIVATION OF THE LAGRANGIAN DENSITY

In the local coordinate system, the Néel vector $\mathbf{n}$ reads $\mathbf{n}' = (\delta_x, \delta_y, \delta_z)$, with $\delta_z = (1-\delta_x^2-\delta_y^2)^{1/2}$. Here, the rotation matrix component is given by $\mathbf{T}_{ij} = 2P_iP_j - \delta_{ij}$, with $i = 1, 2, 3$, the vector [23,47]

$$\mathbf{P} = \left(\sin\frac{\theta}{2}\cos\varphi, \sin\frac{\theta}{2}\sin\varphi, \cos\frac{\theta}{2}\right), \tag{B1}$$

and the Dirac delta function δ_{ij}. The Berry phase term is given by

$$L_b = \frac{\rho_0^2\dot{\mathbf{n}}^2}{2A_0} = \frac{\rho_0^2[(\partial_t + i\mathbf{A})\mathbf{n}']^2}{2A_0}, \tag{B2}$$

where $\mathbf{A} = \mathbf{T}^{-1}\partial_t\mathbf{T}$. Substituting $\mathbf{n}'$ into Eq. (B2) and conserving the second order in the fluctuation field, one obtains the Berry phase

$$L_b = \frac{\rho_0^2[(1-\psi^*\psi)\dot{\mathbf{n}}_0^2 + i(\psi^*\partial_t\psi - \psi\partial_t\psi^*)\cos\theta\partial_t\varphi + \partial_t\psi^*\partial_t\psi]}{2A_0}, \tag{B3}$$

and the Hamiltonian density is [25]

$$u_{\text{total}} = u_0 + \frac{iA^*(\psi^*\nabla\psi - \psi\nabla\psi^*)\boldsymbol{a}_{\text{total}}}{2} - \psi^*\psi u_0 + \frac{A^*\partial_i\psi^*\partial_i\psi}{2} - \frac{K\psi^*\psi}{2}. \tag{B4}$$

[1] T. H. R. Skyrme, Nucl. Phys. **31**, 556 (1962).
[2] Z. Hou, Q. Zhang, X. Zhang, G. Xu, J. Xia, B. Ding, H. Li, S. Zhang, N. M. Batra, and P. M. Costa, Adv. Mater. **32**, 1904815 (2020).
[3] Z. Hou, Q. Zhang, G. Xu, S. Zhang, C. Gong, B. Ding, H. Li, F. Xu, Y. Yao, and E. Liu, ACS Nano **13**, 922 (2019).
[4] X. Z. Yu, Y. Onose, N. Kanazawa, J. H. Park, J. H. Han, Y. Matsui, N. Nagaosa, and Y. Tokura, Nature (London) **465**, 901 (2010).
[5] X. Yu, N. Kanazawa, Y. Onose, K. Kimoto, W. Zhang, S. Ishiwata, Y. Matsui, and Y. Tokura, Nat. Mater. **10**, 106 (2011).
[6] S. Mühlbauer, B. Binz, F. Jonietz, C. Pfleiderer, A. Rosch, A. Neubauer, R. Georgii, and P. Böni, Science **323**, 915 (2009).
[7] S. X. Huang and C. L. Chien, Phys. Rev. Lett. **108**, 267201 (2012).
[8] L. J. Bannenberg, H. Wilhelm, R. Cubitt, A. Labh, M. P. Schmidt, E. Lelièvre-Berna, C. Pappas, M. Mostovoy, and A. O. Leonov, npj Quantum Mater. **4**, 11 (2019).
[9] S. D. Pollard, J. A. Garlow, J. Yu, Z. Wang, Y. Zhu, and H. Yang, Nat. Commun. **8**, 14761 (2017).
[10] S. Heinze, K. Von Bergmann, M. Menzel, J. Brede, A. Kubetzka, R. Wiesendanger, G. Bihlmayer, and S. Blügel, Nat. Phys. **7**, 713 (2011).
[11] O. Boulle, J. Vogel, H. Yang, S. Pizzini, D. de Souza Chaves, A. Locatelli, T. O. Menteş, A. Sala, L. D. Buda-Prejbeanu, and O. Klein, Nat. Nanotechnol. **11**, 449 (2016).
[12] E. Mascot, J. Bedow, M. Graham, S. Rachel, and D. K. Morr, npj Quantum Mater. **6**, 6 (2021).
[13] R. Tomasello, E. Martinez, R. Zivieri, L. Torres, M. Carpentieri, and G. Finocchio, Sci. Rep. **4**, 6784 (2014).
[14] J. Iwasaki, M. Mochizuki, and N. Nagaosa, Nat. Commun. **4**, 1463 (2013).
[15] J. Liang, J. Yu, J. Chen, M. Qin, M. Zeng, X. Lu, X. Gao, and J. M. Liu, New J. Phys. **20**, 053037 (2018).
[16] H. Y. Yuan, X. S. Wang, M.-H. Yung, and X. R. Wang, Phys. Rev. B **99**, 014428 (2019).
[17] X. Wang, W. L. Gan, J. Martinez, F. N. Tan, M. Jalil, and W. S. Lew, Nanoscale **10**, 733 (2018).
[18] J. Iwasaki, A. J. Beekman, and N. Nagaosa, Phys. Rev. B **89**, 064412 (2014).
[19] C. Psaroudaki and D. Loss, Phys. Rev. Lett. **120**, 237203 (2018).
[20] L. Kong and J. Zang, Phys. Rev. Lett. **111**, 067203 (2013).
[21] X. Zhang, M. Ezawa, D. Xiao, G. Zhao, Y. Liu, and Y. Zhou, Nanotechnology **26**, 225701 (2015).
[22] Y. Jiang, H. Y. Yuan, Z.-X. Li, Z. Wang, H. W. Zhang, Y. Cao, and P. Yan, Phys. Rev. Lett. **124**, 217204 (2020).
[23] Y.-T. Oh, H. Lee, J.-H. Park, and J. H. Han, Phys. Rev. B **91**, 104435 (2015).
[24] X. Zhang, J. Müller, J. Xia, M. Garst, X. Liu, and Y. Zhou, New J. Phys. **19**, 065001 (2017).
[25] J. Stigloher, T. Taniguchi, H. S. Körner, M. Decker, T. Moriyama, T. Ono, and C. H. Back, Phys. Rev. Lett. **121**, 137201 (2018).
[26] Y. Wang, D. Zhu, Y. Yang, K. Lee, R. Mishra, G. Go, S.-H. Oh, D.-H. Kim, K. Cai, and E. Liu, Science **366**, 1125 (2019).
[27] J. Lan and J. Xiao, Phys. Rev. B **103**, 054428 (2021).
[28] C. Schütte and M. Garst, Phys. Rev. B **90**, 094423 (2014).
[29] X. Zhang, Y. Zhou, and M. Ezawa, Nat. Commun. **7**, 10293 (2016).
[30] X. Zhang, Y. Zhou, and M. Ezawa, Sci. Rep. **6**, 24795 (2016).
[31] W. Legrand, D. Maccariello, F. Ajejas, S. Collin, A. Vecchiola, K. Bouzehouane, N. Reyren, V. Cros, and A. Fert, Nat. Mater. **19**, 34 (2020).
[32] S. Gao, H. D. Rosales, F. A. Gómez Albarracín, V. Tsurkan, G. Kaur, T. Fennell, P. Steffens, M. Boehm, P. Čermák, A. Schneidewind, E. Ressouche, D. C. Cabra, C. Rüegg, and O. Zaharko, Nature (London) **586**, 37 (2020).
[33] J. Barker and O. A. Tretiakov, Phys. Rev. Lett. **116**, 147203 (2016).
[34] H. Xia, C. Jin, C. Song, J. Wang, J. Wang, and Q. Liu, J. Phys. D **50**, 505005 (2017).
[35] L. Shen, J. Xia, G. Zhao, X. Zhang, M. Ezawa, O. A. Tretiakov, X. Liu, and Y. Zhou, Phys. Rev. B **98**, 134448 (2018).
[36] X. Chen, X. Zhou, R. Cheng, C. Song, J. Zhang, Y. Wu, Y. Ba, H. Li, Y. Sun, and Y. You, Nat. Mater. **18**, 931 (2019).
[37] H. Yu, J. Xiao, and H. Schultheiss, Phys. Rep. **905**, 1 (2021).
[38] M. W. Daniels, R. Cheng, W. Yu, J. Xiao, and D. Xiao, Phys. Rev. B **98**, 134450 (2018).
[39] M. W. Daniels, W. Yu, R. Cheng, J. Xiao, and D. Xiao, Phys. Rev. B **99**, 224433 (2019).
[40] W. Yu, J. Lan, and J. Xiao, Phys. Rev. B **98**, 144422 (2018).
[41] J. Lan, W. Yu, and J. Xiao, Nat. Commun. **8**, 178 (2017).
[42] A. Qaiumzadeh, L. A. Kristiansen, and A. Brataas, Phys. Rev. B **97**, 020402(R) (2018).
[43] Z. Jin, T. T. Liu, W. H. Li, X. M. Zhang, Z. P. Hou, D. Y. Chen, Z. Fan, M. Zeng, X. B. Lu, X. S. Gao, M. H. Qin, and J.-M. Liu, Phys. Rev. B **102**, 054419 (2020).
[44] V. Baltz, A. Manchon, M. Tsoi, T. Moriyama, T. Ono, and Y. Tserkovnyak, Rev. Mod. Phys. **90**, 015005 (2018).
[45] R. Khoshlahni, A. Qaiumzadeh, A. Bergman, and A. Brataas, Phys. Rev. B **99**, 054423 (2019).
[46] Z. Y. Chen, M. H. Qin, and J.-M. Liu, Phys. Rev. B **100**, 020402(R) (2019).
[47] S. K. Kim, Y. Tserkovnyak, and O. Tchernyshyov, Phys. Rev. B **90**, 104406 (2014).
[48] K. A. van Hoogdalem, Y. Tserkovnyak, and D. Loss, Phys. Rev. B **87**, 024402 (2013).
[49] S. K. Kim, K. Nakata, D. Loss, and Y. Tserkovnyak, Phys. Rev. Lett. **122**, 057204 (2019).
[50] G. Tatara, H. Kohno, and J. Shibata, Phys. Rep. **468**, 213 (2008).
[51] V. K. Dugaev, P. Bruno, B. Canals, and C. Lacroix, Phys. Rev. B **72**, 024456 (2005).
[52] G. Tatara, Physica E **106**, 208 (2019).
[53] E. G. Tveten, A. Qaiumzadeh, O. A. Tretiakov, and A. Brataas, Phys. Rev. Lett. **110**, 127208 (2013).
[54] S.-H. Oh, S. K. Kim, J. Xiao, and K.-J. Lee, Phys. Rev. B **100**, 174403 (2019).
[55] R. Keesman, M. Raaijmakers, A. E. Baerends, G. T. Barkema, and R. A. Duine, Phys. Rev. B **94**, 054402 (2016).
[56] F. J. dos Santos, M. dos Santos Dias, and S. Lounis, Phys. Rev. B **102**, 104436 (2020).
[57] P. Yan, X. S. Wang, and X. R. Wang, Phys. Rev. Lett. **107**, 177207 (2011).